

Onset of Aftershocks: Constraints on the Rate-and-State Model

Sebastian Hainzl^{1,2} , Morgan T. Page³ , and Nicholas J. van der Elst³ 

Abstract

Aftershock rates typically decay with time t after the mainshock according to the Omori–Utsu law, $R(t) = K(c + t)^{-p}$, with parameters K , c , and p . The rate-and-state (RS) model, which is currently the most popular physics-based seismicity model, also predicts an Omori–Utsu decay with $p = 1$ and a c -value that depends on the size of the coseismic stress change. Because the mainshock-induced stresses strongly vary in space, the c -value should vary accordingly. Short-time aftershock incompleteness (STAI) in earthquake catalogs has prevented a detailed test of this prediction so far, but the newly developed a -positive method for reconstructing the true earthquake rate now allows its testing. Using previously published slip models, we calculate the coseismic stress changes for the six largest mainshocks in Southern California in recent decades and estimate the maximum shear as a scalar proxy of the coseismic stress tensor. Aftershock rates reconstructed for events in different stress ranges show that the rates follow a power law with $p = 1$ independent of stress with no clear sign of a c -value. The onset of the power-law decay is abrupt and more delayed in areas with smaller stress changes. The observations do not necessarily contradict the RS model, as STAI limits the resolution for early aftershocks, and the RS model can reproduce the observations for specific $A\sigma$ values. However, the observations lead to strong constraints, namely $A\sigma < 10$ kPa and a power-law decay of the background rate with distance to the fault, with exponent 2.7.

Cite this article as Hainzl, S., M. T. Page, and N. J. van der Elst (2024). Onset of Aftershocks: Constraints on the Rate-and-State Model, *Seismol. Res. Lett.* **XX**, 1–10, doi: [10.1785/0220240176](https://doi.org/10.1785/0220240176).

Supplemental Material

Introduction


The two most prominent empirical distributions in statistical seismology are the Gutenberg–Richter distribution describing the magnitude distribution and the Omori–Utsu law for the decay of the aftershock rate $R(t)$ as a function of the time t after a major earthquake,

$$R(t) = \frac{K}{(c + t)^{-p}}, \quad (1)$$

in which parameter K scales with the mainshock magnitude. In its original form, the exponent p was 1.0 (Omori, 1894). However, this constraint was later relaxed with observations showing p values typically between 0.8 and 1.2 (Utsu *et al.*, 1995). The observed c usually only reflects the incompleteness of earthquake catalogs after mainshocks when only the largest aftershocks are detected. This was first observed by Kagan (2004), later confirmed by further statistical analyses (Omi *et al.*, 2013; Hainzl, 2016b), and directly proven by detailed waveform analysis (Peng *et al.*, 2006, 2007; Enescu *et al.*, 2007, 2009).

Ignoring the short-time aftershock incompleteness (STAI) of catalogs can strongly bias parameter estimates of statistical

seismicity models, such as aftershock models or the epidemic-type aftershock sequence model, used for time-dependent hazard assessment (Kagan, 2004; Hainzl, 2016a, 2021). However, STAI can also lead to incorrect physical interpretations (Shcherbakov *et al.*, 2004) or can hinder the full exploitation of physics-based seismicity models proposing a stress-dependent aftershock decay function (Dieterich, 1994; Narteau *et al.*, 2005, 2008; Dahm and Hainzl, 2022). These models predict a more delayed power-law onset, that is, a larger c -value of the aftershock decay (equation 1) for small stress changes. The currently most prominent physics-based model is the rate-and-state (RS) model introduced by Dieterich (1994), which properly considers the rate and slip dependence of frictional strength and time-dependent restrengthening observed in laboratory experiments. By considering volumes with populations of frictional instabilities

1. Helmholtz Centre Potsdam Deutsches GeoForschungsZentrum GFZ, Potsdam, Germany,  <https://orcid.org/0000-0002-2875-0933> (SH); 2. Institute of Geosciences, University of Potsdam, Potsdam, Germany; 3. U.S. Geological Survey, Pasadena, California, U.S.A.,  <https://orcid.org/0000-0001-9321-2990> (MTP);  <https://orcid.org/0000-0002-3812-1153> (NJE)

*Corresponding author: hainzl@gfz-potsdam.de

© Seismological Society of America

following the laboratory-derived constitutive friction law, it can explain many aspects of observed earthquake phenomena, such as earthquake clustering and seismic quiescence (see, e.g., Scholz, 1998; Dieterich, 2007; Hainzl *et al.*, 2010; Cattania *et al.*, 2014; Mancini *et al.*, 2019). However, its most important justification is the ability to reproduce the Omori–Utsu decay of aftershocks. It predicts $p = 1.0$ for a single stress step, but for more realistic variable coseismic stress changes, the total aftershock activity decays with $p < 1$ (Helmstetter and Shaw, 2006; Marsan, 2006). The second major aftershock prediction is that c is an exponential function of the stress magnitude. In regions with large stress changes, the power-law decay should start immediately after the mainshock, that is, $c \approx 0$. In contrast, in regions with small coseismic stress changes, the aftershock rate should remain constant for much longer before it starts to decay. Such a different onset of the aftershock activity has not yet been convincingly demonstrated, which might be explained by STAI obscuring the pattern of early aftershocks.

The new a -positive method developed by van der Elst and Page (2023) allows the reconstruction of the true earthquake rate for early aftershocks and thus testing of the RS prediction. The companion article by Page *et al.* (2024) analyzes the rates obtained by this method as a function of the distance to the mainshocks, as a proxy for the coseismic stress changes, and finds that the reconstructed aftershock rates for the M 7.1 Ridgecrest mainshock demonstrate (1) a delay in the onset of the first resolvable aftershock rates that increases with distance and (2) a flattening of the decay for aftershocks at the largest distances. These observations are consistent with the RS prediction.

Here, we also use the a -positive method, but based on published slip models, we directly calculate the coseismic stress changes at the aftershock hypocenters instead of using the distances as a stress proxy. This accounts for the spatially variable mainshock slip and stress pattern and allows a direct comparison of the reconstructed aftershock decay with the RS model prediction for the same stress values. For this purpose, we analyze the aftershock activity of the six largest mainshocks in Southern California in the past few decades using the slip models available in the finite-fault source model (SRCMOD) database (Mai and Thingbaijam, 2014) to calculate the induced stress tensor at the aftershock hypocenters. As a scalar stress, we use the maximum shear (MS) value that has been shown in previous studies to be superior in its predictive power compared to receiver-dependent stress scalars such as Coulomb failure stress changes ΔCFS (Meade *et al.*, 2017; Sharma *et al.*, 2020). The results show an apparent contradiction that aftershocks follow a power law without clear bending (c -value) after their onset, which is delayed for regions with small stress changes. However, we show that the observations are consistent with the RS model when some constraints are satisfied.

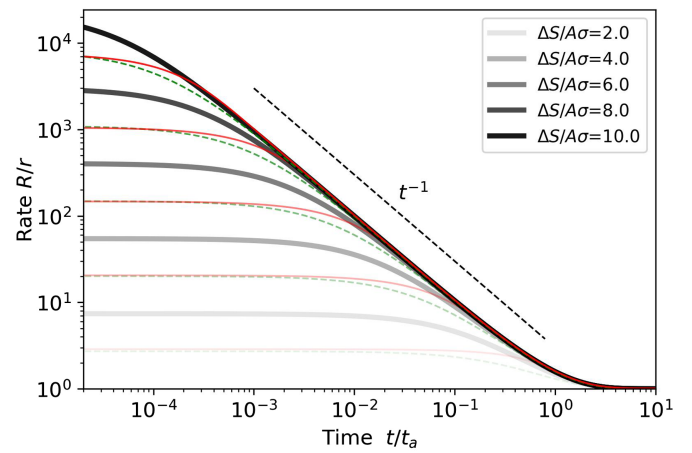


Figure 1. Predictions of the normalized aftershock rates as a function of the normalized time after the mainshock. The rate-and-state (RS) solutions (equation 2; gray bold lines) are compared with the solutions for subcritical initial stresses with $\Delta S_c = A\sigma$: subcritical RS model (green dashed lines) and time-dependent stress response (TDSR) model with uniformly distributed stresses below ΔS_c (red lines). All models predict (1) a maximum constant rate immediately after the mainshock, (2) a c -value depending on the stress change, and (3) the convergence to the same decay rate for all stress changes. The color version of this figure is available only in the electronic edition.

Theory

Assuming that the initial seismicity rate is at a background (reference) level r related to a tectonic background (reference) stressing rate $\dot{\tau}_r$, the RS model (Dieterich, 1994) predicts a seismicity rate R following a positive stress step ΔS at time $t = 0$ according to

$$R(t) = \frac{r}{(e^{-\frac{\Delta S}{A\sigma}} - 1)e^{\frac{t}{t_a}} + 1} \quad \text{for } \dot{S}(t > 0) = \dot{\tau}_r, \quad (2)$$

and

$$R(t) = \frac{rt_a}{t_a e^{-\frac{\Delta S}{A\sigma}} + t} \quad \text{for } \dot{S}(t > 0) = 0, \quad (3)$$

with definition $t_a = A\sigma/\dot{\tau}_r$, which is often called relaxation time or aftershock duration. The model parameter $A\sigma$ is the product of the effective normal stress σ acting on the faults and the dimensionless constitutive friction parameter A , which is usually on the order of 0.01 (Dieterich, 1994, 2007). Equation (3) approximates equation (2) for $t \ll t_a$ and is identical to the Omori–Utsu law with $p = 1$ and $c = t_a \exp(-\Delta S/A\sigma)$. Figure 1 shows equation (2) for different stress steps, highlighting (1) the dependence of c on ΔS , (2) the rolloff to a power law with $p = 1$, and (3) that the predicted rates finally end in the same values independent of ΔS .

Heimisson and Segall (2018) reformulated the RS model based on the time to instability for a population of sources

and eschewed the seismicity state variable. However, they finally derived the same main solutions. Heimisson *et al.* (2022) extended the model to subcritical initial stress conditions. In this case, the initial condition is such that all sources are in the healing phase, that is, they are inactive, unless the stress is increased by ΔS_c . The solution for a stress step ΔS is the same as that of the RS model (equations 2 and 3), only with a reduced step $\Delta S - \Delta S_c$ (equation 4; Heimisson *et al.* 2022). Thus, the subcritical RS model also predicts the maximum rate immediately after the mainshock.

The recently introduced time-dependent stress response (TDSR) model (Dahm and Hainzl, 2022) can be seen as a generalization of the RS models. It is based on the assumption that the mean time-to-failure depends exponentially on the stress state,

$$\bar{t}_f = t_0 e^{-(S-S_0)/\delta\sigma}, \quad (4)$$

with constants $\delta\sigma$, S_0 , and t_0 describing the stress sensitivity $\delta\sigma$ (equivalent to $A\sigma$ of the RS model) and the mean failure time t_0 at an applied reference stress S_0 . RS friction leads to the same relationship that ultimately determines the response of seismicity. However, this relation cannot be only a consequence of the dynamics of a slider with an RS-dependent friction law, but such an exponential function has also been widely used to study subcritical crack growth and brittle failure in geological materials under both tensional stresses (Aktinson, 1984) and compressional (shear) stresses (Scholz, 1968; Ohnaka, 1983). In contrast to RS, the initial stress distribution of the seismic sources is explicitly considered in the evolution equations of the TDSR model. Using the assumption of a critical initial condition, in which background stressing leads to a constant background rate r , as assumed implicitly for the solutions of the RS model, the TDSR model solutions are identical to those of the RS model, as shown by Dahm and Hainzl (2022). Thus, all solutions of the TDSR model for critical initial conditions can be interpreted as solutions of the RS model and vice versa. However, the TDSR model offers the flexibility to study the response (also RS response) for different initial stress distributions, in particular realistic subcritical stress distributions.

Figure 1 shows the predicted aftershock rates for different stress steps in the case of the RS and TDSR models with a subcritical stress state (thin lines) in comparison to RS (bold lines). The result shows that subcriticality does not lead to an initial gap of aftershocks. As mentioned earlier, subcritical RS models yield the solutions of RS (equations 2 and 3) with a reduced stress step. Therefore, it also predicts a constant rate for early aftershocks (green curves in Fig. 1). Similarly, using the TDSR model with a uniform distribution of stress states below $S_0 - \Delta S_c$ yields a maximum aftershock rate at the mainshock time (red curves in Fig. 1).

Because of the lack of detailed information about the initial stress and the similarity of aftershock patterns for different

initial stress states, we assume critical initial conditions in the following analysis and use the RS model.

Method

Even in periods with constant network configuration, recording algorithm, and environment noise condition, the M_c level increases during high-seismic activity, such as in the first days of an aftershock sequence following a mainshock (Kagan, 2004) or intense swarm activity (Hainzl, 2016b). If not correctly considered, those short-term M_c fluctuations bias the estimations of essential seismicity parameters for seismic hazard assessment, such as the b -value of the frequency-magnitude distribution and the aftershock rate (Kagan, 2004). van der Elst (2021) and van der Elst and Page (2023) developed new methods based on magnitude (b -positive) and time (a -positive) differences to estimate the b -value and the true earthquake rate robustly for time-varying completeness.

According to the a -positive method, for selected aftershocks with occurrence times t_i and magnitudes m_i in the period $[0, T]$, point estimates of the rates are given by

$$r_i = \frac{n_i}{\tau_i}, \quad (5)$$

in which $\tau_i = \Delta t_i 10^{-b^+(m_i + \delta M_c - M_{\text{ref}})}$ for a given reference magnitude M_{ref} . If a subsequent event exceeds the magnitude of the earthquake by δM_c , $n_i = 1$ and $\Delta t_i = \min\{t_j | j > i \text{ and } m_j \geq m_i + \delta M_c\} - t_i$. If not, $n_i = 0$ and $\Delta t_i = T - t_i$. The corresponding time of the point rate estimate is set to the mean of the interval, namely $t_{r,i} = t_i + 0.5\Delta t_i$. Smoothed rates are determined by selecting the N_n nearest events of event i in time ($t_{r,k}$ with their corresponding n_k values, $k = 1, \dots, N_n$) and determining the corresponding time t_i^+ and rate r_i^+ by

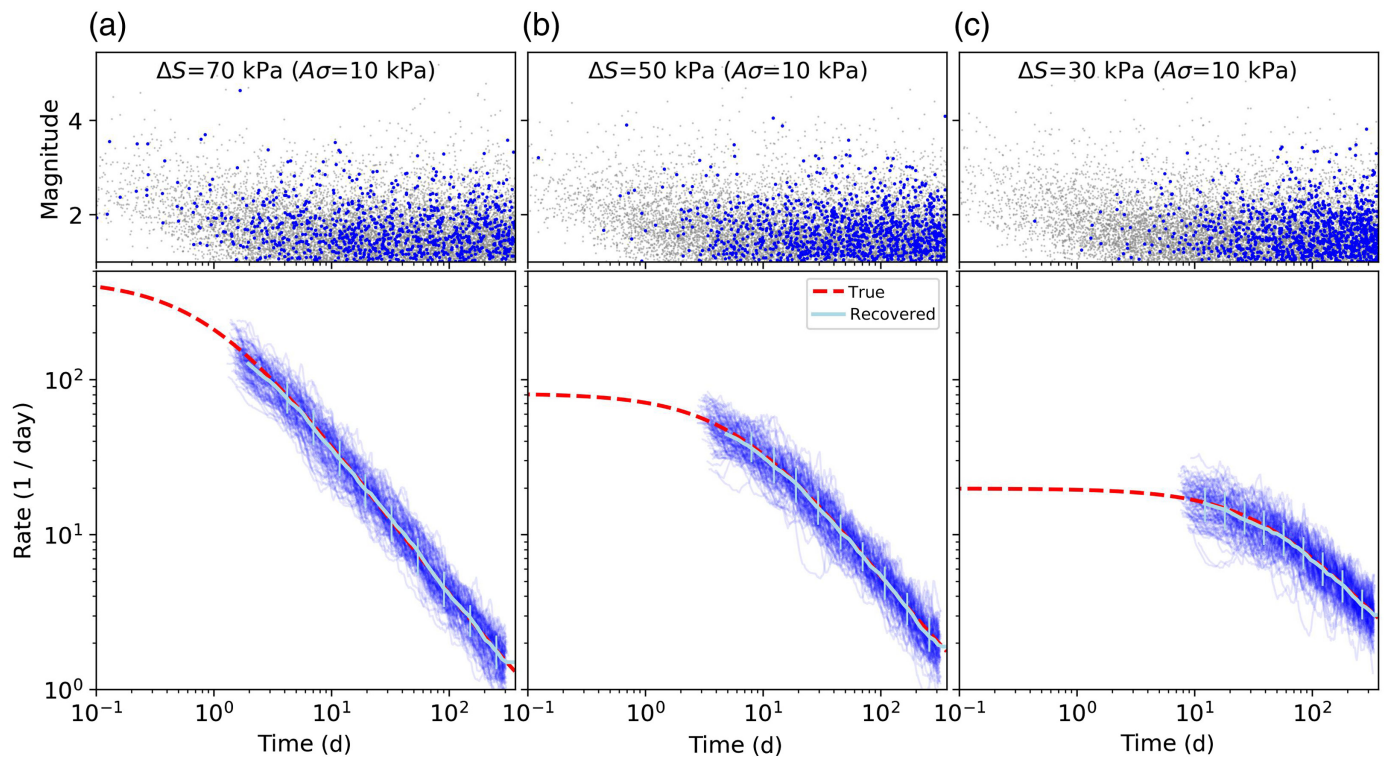
$$t_i^+ = \frac{1}{N_n} \sum_{k=1}^{N_n} t_{r,k}, \quad (6)$$

$$r_i^+ = \sum_{k=1}^{N_n} n_k \left(\sum_{k=1}^{N_n} \tau_k \right)^{-1}. \quad (7)$$

In our study, we use b -positive and a -positive methods to estimate the b -value (b^+) and the earthquake rate (r^+) as a function of the coseismic stress changes, for which we consistently use $m \geq 1.0$ aftershocks, $M_{\text{ref}} = 1.0$, and $\delta M_c = 0.4$.

Test for RS simulations

We first apply the approach to synthetic simulations with realistic incompleteness to test its ability to recover the true aftershock rates in a subregion of the aftershock zone. For this purpose, we perform Monte Carlo simulations of the RS model (equation 2) with $A\sigma = 10$ kPa, $t_a = 1000$ days, and a



Gutenberg–Richter value of $b = 1.0$, in which r is set to achieve a certain number of observable events. The simulations consist of two different distributions that include, on average, (1) 1000 observable target aftershocks using either a stress step of 70, 50, or 30 kPa and (2) 10,000 observable adjacent aftershocks using $\Delta S = 100$ kPa. To account for realistic incompleteness, each simulation is filtered to account for (1) network insufficiency and (2) STAI. The first is done by randomly removing small magnitude events using an error function, that is, the integral of a normal distribution, as the detection probability function (Ogata and Katsura, 1993). Here, we use a mean value of $\mu = 1.4$ and a standard deviation of $\tilde{\sigma} = 0.4$, meaning that events with magnitudes of 1.4 and 2.0 have a chance of 50% and 93%, respectively, to be detected. The second is done by removing all events that occurred with less than the blind time $T_b = 100$ s after a larger event, according to results by Hainzl (2021) for the same Californian mainshocks. In this way, earthquakes in the adjacent region can prevent the observation of target events, as expected for real sequences. After considering incompleteness, each simulation consists of 10% target events out of the total set of about 11,000 observable aftershocks. The event rates at later times are greater for smaller stress steps (with correspondingly greater c -value) to end up with the same total number of events.

Figure 2 shows an example sequence and the reconstructed aftershock rate for 100 Monte Carlo simulations for each of the three different stress steps in the target region. In all cases, the method is found to provide unbiased estimates of the true rate, confirming that the a -positive method can be used to estimate the true rate for a subset of the aftershock activity. However,

Figure 2. Test for RS simulations ($A\sigma = 10$ kPa, $t_a = 1000$ days, $b = 1.0$) consisting of about 1000 observable target events (blue points in the top panels) and 10,000 observable events in adjacent regions (gray) after accounting for catalog incompleteness. (a–c) Different stress steps 70, 50, and 30 kPa in the target region, respectively. For each case, the upper plot shows an example catalog and the lower plot shows the estimated rates for 100 random simulations (blue thin line) and their root mean square errors (light blue error bars) using $N_n = 100$. The mean value of these estimates (light blue bold line) agrees well with the true rate (red dashed line). The color version of this figure is available only in the electronic edition.

due to STAI, the bending related to the c -value cannot be recovered for $\Delta S = 70$ kPa and is also almost invisible for $\Delta S = 50$ kPa. The bending is only partially visible for the smallest stress step.

Data Mainshocks

The six largest earthquakes, so-called mainshocks, which occurred within the box defined by $[32.0^\circ \text{ N}, 36.5^\circ \text{ N}]$ and $[-121.0^\circ \text{ W}, -115.0^\circ \text{ W}]$ in the past 50 yr are selected. These mainshocks are the 1987 M 6.6 Superstition Hill, the 1992 M 7.3 Landers, the 1994 M 6.7 Northridge, the 1999 M 7.1 Hector Mine, the 2010 M 7.2 Baja California, and the 2019 M 7.1 Ridgecrest events.

Slip models and stress calculations

All 22 slip models available in the SRCMOD database (Mai and Thingbaijam, 2014) are selected. These are six models for

Northridge, five models for Landers, four models for Hector Mine, three models for Ridgecrest, and two models for the Baja California and Superstition Hill mainshocks. All slip models and related references are provided in Table S1, available in the supplemental material to this article.

For each of the mainshocks, the target space–time volume is defined by (1) a rectangular area in latitude–longitude with an extension of 100 km from the epicenter and (2) a depth extension of 30 km, with a grid spacing of 1 km in all directions, leading to a total of 1.2×10^6 grid points for each mainshock. For each slip model and grid point, the stress tensor is calculated assuming a homogeneous half-space with a Poisson's ratio of 0.25 and a shear modulus of 30 GPa. As the stress scalar, we use MS related to the coseismic stress changes because it has been shown in previous studies that it is the best predictor (together with Van Mises stress) of the spatial location and density of aftershocks (Meade *et al.*, 2017; Sharma *et al.*, 2020). MS is always positive and calculated by $(\chi_1 - \chi_3)/2$, in which χ_1 and χ_3 are the largest and smallest eigenvalues of the induced stress tensor, respectively. The final stress value at each grid node is calculated by averaging the results for the alternative slip models. As an example, Figure S1 shows the calculated MS values for all mainshocks at a depth of 9.5 km.

Aftershocks

Aftershocks are selected from the relocated catalog (Hauksson *et al.*, 2012) downloaded from the Southern California Earthquake Data Center (SCEDC) and consist of 800,499 earthquakes recorded between 1 January 1981 and 31 March 2022, in the range of -122° to -113° E and 30° to 38° N. The aftershocks occurring in the grid volume in the first $T = 365$ days after the mainshock are chosen. The events in the target volume are associated with the stress value of the closest grid point. Similarly, we calculate the nearest 3D distance to any fault patch of a slip model for each event and associate the event with the average of those distances for the alternative slip models. To remove background events and secondary aftershocks, that is, aftershocks triggered by other aftershocks, we apply the nearest-neighbor (NN) approach (Zaliapin *et al.*, 2008), which has been demonstrated to be robust with respect to (1) changes in the involved parameters of the method, (2) catalog incompleteness, and (3) location errors (Zaliapin and Ben-Zion, 2013). Here, we use the nearest distance to the fault as the mainshock distance, $b = 1$, and a fractal dimension $d_f = 2.3$ for all sequences to first separate triggered and background events using a threshold of -1.53 (for units in km and days) and then select only those aftershocks for which the mainshock is the nearest event. The selected number of events range from 2889 for Superstition Hill to 23,909 for Ridgecrest and are provided in Table S1.

Results

We follow two different approaches for binning the aftershock region. The first approach is to use preset stress ranges to select

the aftershocks, which leads to a different number of aftershocks in each bin. The second approach is to use frequency binning, that is, choosing nonoverlapping stress bins with an equal number of aftershocks in each bin (see illustration in Fig. S2). For a given bin $[S_1, S_2]$, we calculate (1) the rates using a^+ with b^+ and (2) the total volume of the corresponding region in cubic kilometers, that is, the number of grid points with $S_1 \leq \Delta S < S_2$, enabling the calculation of the earthquake rate density. The reason to independently estimate b for each bin is that b generally depends on the stress change of the mainshock (Sharma *et al.*, 2023). Figure S3 shows the dependence of the estimated b -value on stress in the case of the six mainshocks, indicating a systematic increase in b with stress for $\Delta S \geq 1$ MPa, in general agreement with the average tendency of 127 global mainshocks observed by Sharma *et al.* (2023).

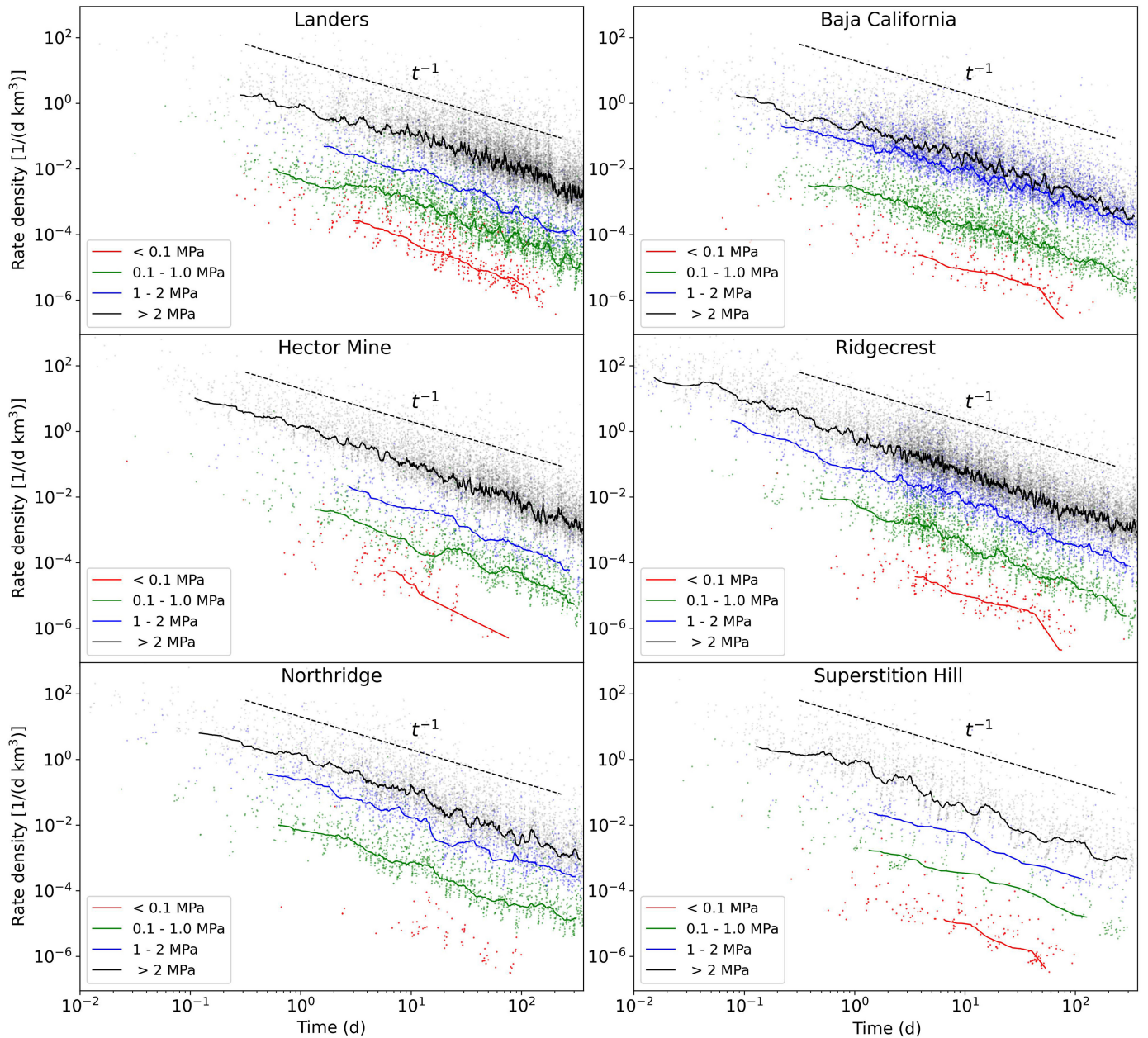
First, we use the fixed stress intervals $\Delta S < 0.1$ MPa, $0.1 \leq \Delta S < 1.0$ MPa, $1 \leq \Delta S < 2$ MPa, and $\Delta S \geq 2$ MPa. The results are shown in Figure 3. The rates reconstructed by the a^+ method do not show any clear signal of a finite c -value, even in regions with small stresses. Instead, the onset of the power-law decay is strongly delayed for the latter.

However, the observed delayed onset for small stress changes might be related to smaller event numbers in the bins with small stresses. To answer this question, we use frequency binning with nonoverlapping frequency bins of N aftershocks in each stress bin. Furthermore, to increase the resolution for regions with small stress changes where a large detectable c -value is expected, we analyze the combined data of all mainshocks instead of analyzing individual sequences. In particular, n_i and τ_i are estimated independently for each sequence, but all data are then combined to calculate the smoothed r^+ curve with N_n neighbor smoothing.

Figure 4a shows the stacked activity of all six sequences. The gap of early aftershocks due to STAI is clearly visible. The standard completeness of the catalog is only recovered after a few days. Figure 4b shows the recovered rates for stress bins with $N = 2000$ events and $N_n = 200$. The rates do not show any clear deviations from the $1/t$ decay for early aftershocks. In addition, the onset does not depend on stress as strongly as in the case of the fixed bins, indicating that the varying numbers in the bins enhanced the effect.

Resulting constraints for RS

Fitting the RS model to the observations leads to important constraints on the model parameters. First, the background rate (number of events per time and volume) must vary in space to explain the observations. Figure 4b shows the fit of the RS model to the observations in different stress bins. The RS model can well approximate the reconstructed rates in different stress bins, indicating that $p = 1$ is satisfied. However, $1/t$ decays are offset, in contrast to the expectations of the RS model with constant r . As shown in Figure 1, the RS model



expects that all $1/t$ decays overlap independently of ΔS if t_a and r are constant. Fitting r to the observation in each stress bin for a given $A\sigma = 2$ kPa and $t_a = 500$ days, the estimated r values span a wide range between 4×10^{-7} and $3 \times 10^{-3} m \geq 1$ events per cubic kilometer and day. Those values show a clear increase with ΔS , but physically more reasonable is that the background rate changes with distance to the fault. Thus, Figure 4c shows the estimated background rates as a function of the mean 3D distance d to the rupture of the aftershocks in each stress bin. The background rates per cubic kilometer and day systematically decrease with increasing distance to the fault and follow a power-law decay with an exponent of 2.68 ± 0.04 .

Our observations also constrain other RS parameters. In particular, the observation that the power-law decay continues until the end requires that $t_a > 365$ days. Furthermore, the

Figure 3. Observation of the aftershock decays for all six mainshocks using fixed stress bins. The point estimates of the rates (equation 5) are shown by dots and the r^+ -estimates (equation 7) are shown by lines, using $N_n = 100$ nearest neighbors for smoothing. The color version of this figure is available only in the electronic edition.

onset time of the power-law decay for the smallest stress bin yields a maximum $A\sigma$ value. To explore the second point in more detail, we calculate the r^+ rates of this smallest bin for alternative choices of N and N_n . Larger N means a larger upper ΔS limit of the bin but more stable estimations. In contrast, smaller N values lead to a higher resolution but less stable results. In particular, we test ΔS values between 50 and 100 kPa, corresponding to N ranging from 541 to 1387, for

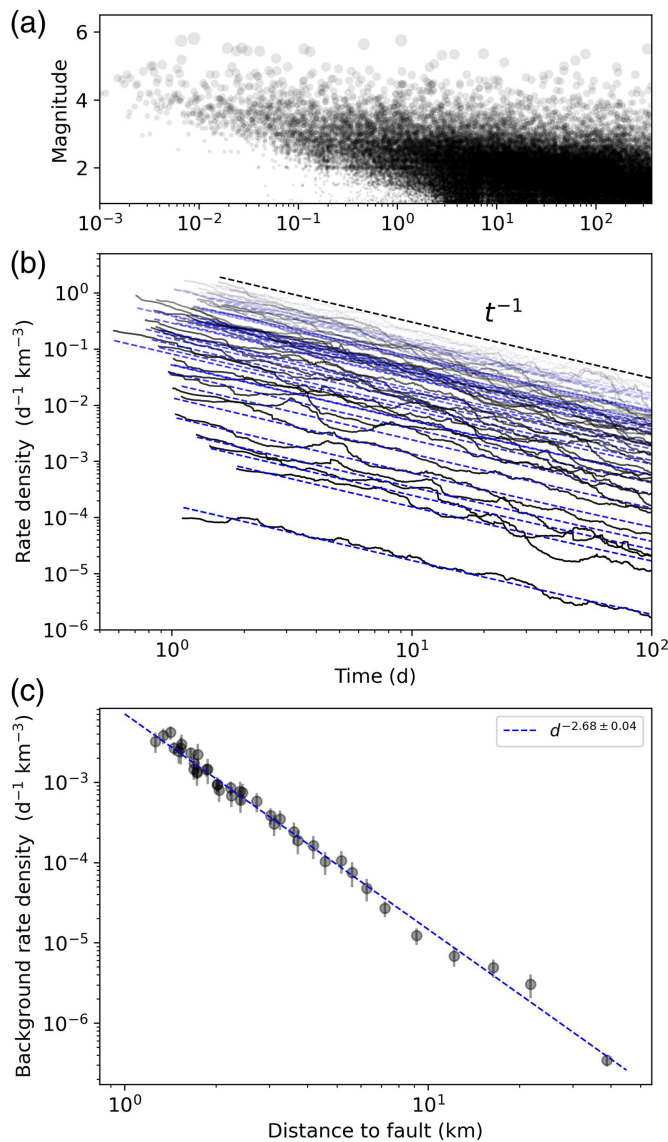


Figure 4. (a) Magnitudes of the stacked activity of the six Californian sequences as a function of the time t after the mainshock. (b) Estimated aftershock rates (r^+ , black solid lines) using nonoverlapping stress bins with $N = 2000$ events and $N_n = 200$. Blue dashed lines represent fits of the RS model (equation 2) to the observations using the observed stress values for ΔS , with $A\sigma = 2$ kPa and $t_a = 500$ days. The background rate r is adapted for each stress bin to fit the observation. (c) The estimated background rate densities r (points) together with their uncertainties (error bars are related to \pm one standard deviation) as a function of the mean 3D distance d to the rupture of the events in the corresponding stress bin. The relation can be well approximated by the dashed line corresponding to an exponent of 2.68 ± 0.04 . The color version of this figure is available only in the electronic edition.

which the NN smoothing is set to $N_n = 0.1N = 54, \dots, 138$. The corresponding r^+ rates are shown in Figure 5a. For each case, we fit a $K/(c+t)$ decay, that is, the Omori-Utsu law with $p = 1$, for times $t < 10$ days, shown as dashed lines on the same plot. According to the RS model, $c = t_a \exp(-\Delta S/A\sigma)$ yielding

$A\sigma = -\Delta S/\ln(c/t_a)$. For a given c , the $A\sigma$ value increases with decreasing t_a and increasing ΔS . Thus, the upper bound of $A\sigma$ is obtained for the minimum t_a value ($t_a = 365$ days) and the upper cutoff of the stress bin (ΔS_{\max}). These estimates are shown together with the results for combinations with more reasonable parameters, that is, the mean stress value $\langle \Delta S \rangle$ and $t_a = 1000$ days. However, the c -value from the fit is rather uncertain due to the rate uncertainties and lack of bending. Therefore, we also use the onset time as an upper estimate of c . Both alternative estimates are shown in Figure 5b. The results indicate a maximum $A\sigma$ value on the order of 10 kPa for more stable results with the largest bin size. Relying on the less stable results for smaller bin sizes yields maximum $A\sigma$ values in the order of only 5 kPa.

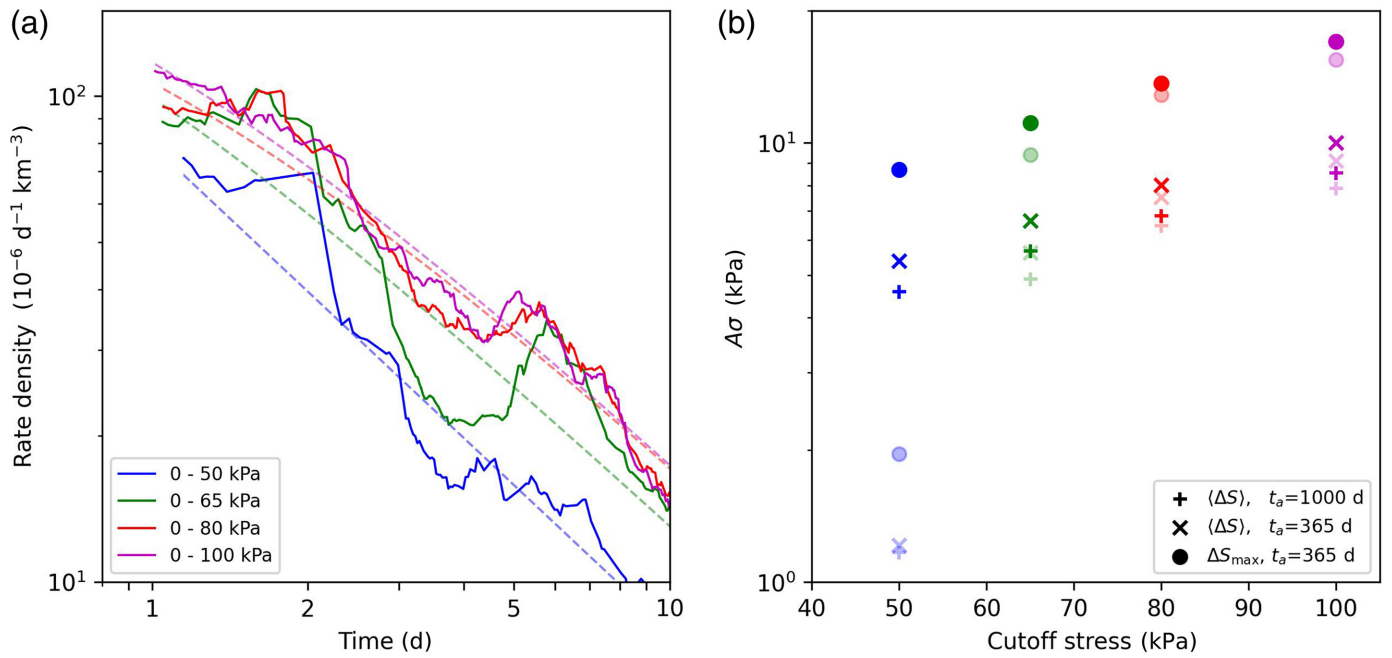
Discussion

Instead of variations in the background rate r , varying t_a values could alternatively explain the lower aftershock densities in more distant regions (see equation 3). In this case, $t_a = A\sigma/\dot{\tau}_r$ should be smaller in more distant regions, implying either a smaller $A\sigma$ or a larger tectonic stressing rate $\dot{\tau}_r$. However, it is not easy to explain why $A\sigma$ should systematically decrease with distance to the fault because it is the product of the nondimensional friction parameter A and the effective normal stress σ on the aftershock faults. Similarly, it is counterintuitive that the tectonic stressing rate increases with distance to the main faults.

A power-law decay $r \sim (\tilde{d} + d)^{-\gamma}$ of the background rates with distance d normal to the fault planes has already been observed by Powers and Jordan (2010), who analyzed declustered seismicity in California. In most cases, they found a small rolloff distance $\tilde{d} < 1$ km in agreement with this study. However, the previous analysis found mostly smaller decay exponents γ in Southern California ranging from 0.9 to 1.9. It requires further research to understand whether the difference might be related to different catalogs or definitions of the faults.

Using the estimated maximum $A\sigma$ value and the lower bound of t_a , the resulting tectonic stressing rate ($\dot{\tau}_r = A\sigma/t_a$) is only on the order of 5–10 kPa/yr or less. Parsons (2006) found peak differential stressing rates (≥ 5 kPa/yr) in a ~ 200 km wide band along the San Andreas fault zone. However, the Landers, Hector Mine, and Ridgecrest mainshocks, for example, occurred in regions with significantly lower stressing rates. Thus, the estimated upper bound on the $\dot{\tau}_r$ value required for the RS fits does not contradict geodetic observations.

MS has been chosen in this study because recent publications show its superiority to Coulomb failure stress estimates, which rely on uncertain definitions of the aftershock mechanisms (Meade et al., 2017; Sharma et al., 2020). MS is the shear stress change achieved for faults optimally oriented to the stress change tensor. Thus, it neglects the existing background stress field, which could bias our estimates. MS represents an upper bound of the shear stress changes; consequently, the



same holds for the $A\sigma$ estimates in this study. Small $A\sigma$ values of 0.8 and 0.4–1.2 kPa have also been previously estimated for reservoir-triggered seismicity at Val d’Agri in Italy and the 2020 Westmorland swarm in California (Rinaldi *et al.*, 2020; Sirorattanakulet *et al.*, 2022), but most previous estimates of $A\sigma$ are higher than the estimates in the present study, for example, $A\sigma = 20$ kPa for the 1992 M_w 7.3 Landers earthquake (Hainzl *et al.*, 2009), $A\sigma = 35 \pm 15$ kPa for the 1995 M_w 6.9 Kobe earthquake (Toda *et al.*, 1998; Stein, 1999), $A\sigma = 10$ kPa for the 2000 Izu earthquake swarm (Toda *et al.*, 2002), $A\sigma = 40$ kPa for the 1997 Umbria–Marche sequence in central Italy (Catalli *et al.*, 2008), $A\sigma = 12$ kPa for the seismicity between 1970 and 2003 in Japan (Console *et al.*, 2006), $A\sigma = 18$ and 4 kPa for the Tohoku and Parkfield sequences (Cattania *et al.*, 2014), and $A\sigma \approx 20$ kPa for the 2016–2017 Central Italy earthquake cascade (Mancini *et al.*, 2019). However, because the new methodology was not available before, the results of the previous studies may suffer in part from the incompleteness of the analyzed data. In particular, the missing early aftershocks, if not fully accounted for, can lead to an underestimated rate of immediate aftershocks, which can be modeled with a larger $A\sigma$ than the true rate.

One possible explanation for the small $A\sigma$ values needed to fit the observations are that $A\sigma$ is likely not constant in reality but has distributed values due to the variability in frictional properties and effective normal stress. The immediate response is driven by the smallest values of such a distribution. A broad $A\sigma$ distribution can lead to negligible c even for a large mean value of $A\sigma$, as shown for a simple synthetic case in Figure S4.

The low $A\sigma$ estimate could also be biased by considering only coseismic static stress changes. Other mechanisms could lead to higher stress changes and, thus, a higher $A\sigma$ value. Dynamic triggering associated with seismic waves from the

Figure 5. Detailed analysis of the onset of the aftershock decay for the region with the smallest ΔS values. (a) The reconstructed aftershock rates (solid lines) using different upper bounds ΔS_{\max} . The corresponding number of aftershocks in the bins ranges from 541 to 1387, for which we set $N_n = 0.1N$. The results show an almost abrupt onset of the $1/t$ decay, indicating that the true c -value must be on the order or shorter than the onset time. The dashed lines refer to the fit of the Omori–Utsu law with $p = 1.0$ to directly estimate the c -value. (b) Estimates of $A\sigma$ as a function of ΔS_{\max} , using $A\sigma = -\Delta S / \ln(c/t_a)$ (see equation 3). The estimate using c equal to the onset time is indicated in bold. The result using the fitted c -value is indicated in paler colors. The points mark the parameter choice that maximizes $A\sigma$ ($t_a = 365$ d and $\Delta S = \Delta S_{\max}$), whereas crosses refer to more reasonable parameter choices (see legend). The color version of this figure is available only in the electronic edition.

mainshocks could be responsible for some of the observed aftershocks, especially in the more distant regions. However, dynamic stress is less effective than static stress in triggering earthquakes according to the RS model (Hainzl *et al.*, 2013). Furthermore, the systematic $d^{-2.7}$ decay of the background rate suggests one dominant mechanism operating at all distances, likely coseismic static stress changes. Postseismic deformations such as afterslip and poroelastic or viscoelastic relaxation could also modify the coseismic stress changes. However, these mechanisms are expected to be less effective on the timescales of the early aftershocks (Cattania *et al.*, 2015). Thus, the MS estimates may reflect the correct size of the effective stress changes.

Finally, as mentioned in the Theory section, the inverted $A\sigma$ value does not necessarily have to be interpreted in terms of the RS-dependent friction law derived from laboratory experiments. Instead, it can be interpreted more generally as the

$\delta\sigma$ parameter in equation (4), describing the scaling of the mean time-to-failure with applied stress.

Conclusion

The RS model is the most popular physics-based seismicity model, predicting an Omori–Utsu decay with $p = 1$ and a stress-dependent c -value. Short-term incompleteness of aftershock catalogs has prevented detailed testing of these predictions so far. However, the new b^+ and a^+ methods now allow the reconstruction of the true aftershock rates and test the predictions of the RS model in more detail.

The systematic analysis of the aftershock sequences of the six largest earthquakes in California in the past few decades shows that RS based on coseismic stress changes can explain the observed decay for different stress changes. Although the RS model is, in principle, consistent with the observations, the study reveals some important constraints on the model parameters, namely that $\Delta\sigma < 10$ kPa and that the background rate decreases with distance from the mainshock fault according to a power law with an exponent of 2.7. Whether these constraints are realistic may be verified by future studies.

Data and Resources

The Southern California earthquake catalog was downloaded from the Southern California Earthquake Data Center (SCEDC; <https://scedc.caltech.edu/data/alt-2011-dd-hauksson-yang-shearer.html>) and all slip models were downloaded from the SRCMOD database (<http://equake-rc.info/srcmod/>). Both websites were last accessed in January 2024.

Declaration of Competing Interests

The authors acknowledge that there are no conflicts of interest recorded.

Acknowledgments

The authors thank Karen Felzer for helpful discussions on the methods and results. The authors also thank Editor-in-Chief Allison Bent, Shinji Toda, and Andrea Llenos for their reviews that helped to improve the article.

References

- Atkinson, B. (1984). Subcritical crack growth in geological materials, *J. Geophys. Res.* **89**, no. B6, 4077–4114.
- Catalli, F., M. Cocco, R. Console, and L. Chiaraluce (2008). Modeling seismicity rate changes during the 1997 Umbria-Marche sequence (central Italy) through rate- and state-dependent model, *J. Geophys. Res.* **113**, no. B11, doi: [10.1029/2007JB005356](https://doi.org/10.1029/2007JB005356).
- Cattania, C., S. Hainzl, L. Wang, B. Enescu, and F. Roth (2015). Aftershock triggering by postseismic stresses: A study based on Coulomb rate-and-state models, *J. Geophys. Res.* **120**, 2388–2407.
- Cattania, C., S. Hainzl, L. Wang, F. Roth, and B. Enescu (2014). Propagation of Coulomb stress uncertainties in physics-based aftershock models, *J. Geophys. Res.* **119**, 7846–7864.
- Console, R., M. Murru, and F. Catalli (2006). Physical and stochastic models of earthquake clustering, *Tectonophysics* **417**, 141–153.
- Dahm, T., and S. Hainzl (2022). A Coulomb stress response model for time-dependent earthquake forecasts, *J. Geophys. Res.* **127**, e2022JB024443, doi: [10.1029/2022JB024443](https://doi.org/10.1029/2022JB024443).
- Dieterich, J. (1994). A constitutive law for rate of earthquake production and its application to earthquake clustering, *J. Geophys. Res.* **99**, 2601–618.
- Dieterich, J. (2007). Applications of rate- and state-dependent friction to models of fault slip and earthquake occurrence, in *Earthquake Seismology, Treatise on Geophysics*, G. Schubert (Editor), Vol. 4, Elsevier, 107–129.
- Enescu, B., J. Mori, and M. Miyazawa (2007). Quantifying early aftershock activity of the 2004 mid-Niigata Prefecture earthquake (Mw6.6), *J. Geophys. Res.* **112**, no. B4, doi: [10.1029/2006JB004629](https://doi.org/10.1029/2006JB004629).
- Enescu, B., J. Mori, M. Miyazawa, and Y. Kano (2009). Omori–Utsu law c -values associated with recent moderate earthquakes in Japan, *Bull. Seismol. Soc. Am.* **99**, no. 2A, 884–891.
- Hainzl, S. (2016a). Apparent triggering function of aftershocks resulting from rate-dependent incompleteness of earthquake catalogs, *J. Geophys. Res.* **121**, 6499–6509.
- Hainzl, S. (2016b). Rate-dependent incompleteness of earthquake catalogs, *Seismol. Res. Lett.* **87**, 337–344.
- Hainzl, S. (2021). ETAS-approach accounting for short-term incompleteness of earthquake catalogs, *Bull. Seismol. Soc. Am.* **112**, 494–507.
- Hainzl, S., B. Enescu, M. Cocco, J. Woessner, F. Catalli, R. Wang, and F. Roth (2009). Aftershock modeling based on uncertain stress calculations, *J. Geophys. Res.* **114**, no. B5, doi: [10.1029/2008JB006011](https://doi.org/10.1029/2008JB006011).
- Hainzl, S., D. Steacy, and S. Marsan (2010). Seismicity models based on Coulomb stress calculations, *Community Online Resource for Statistical Seismicity Analysis*, available at <http://www.corsaa.org> (last accessed March 2024).
- Hainzl, S., O. Zakharova, and D. Marsan (2013). Impact of aseismic transients on the estimation of aftershock productivity parameters, *Bull. Seismol. Soc. Am.* **103**, no. 3, 1723–1732.
- Hauksson, E., W. Yang, and P. Shearer (2012). Waveform relocated earthquake catalog for southern California (1981 to 2011), *Bull. Seismol. Soc. Am.* **102**, 2239.
- Heimisson, E. R., and P. Segall (2018). Constitutive law for earthquake production based on rate-and-state friction: Dieterich 1994 revisited, *J. Geophys. Res.* **123**, 4141–4156.
- Heimisson, E. R., J. D. Smith, J.-P. Avouac, and S. J. Bourne (2022). Coulomb threshold rate-and-state model for fault reactivation: Application to induced seismicity at Groningen, *Geophys. J. Int.* **228**, 2061–2072.
- Helmstetter, A., and B. E. Shaw (2006). Relation between stress heterogeneity and aftershock rate in the rate-and-state model, *J. Geophys. Res.* **111**, no. B7, doi: [10.1029/2005JB004077](https://doi.org/10.1029/2005JB004077).
- Kagan, Y. Y. (2004). Short-term properties of earthquake catalogs and models of earthquake source, *Bull. Seismol. Soc. Am.* **94**, 1207–1228.
- Mai, P. M., and K. K. S. Thingbaijam (2014). SRCMOD: An online database of finite-fault rupture models, *Seismol. Res. Lett.* **85**, no. 6, 1348–1357.
- Mancini, S., M. Segou, M. J. Werner, and C. Cattania (2019). Improving physics-based aftershock forecasts during the 2016–2017 Central Italy earthquake cascade, *J. Geophys. Res.* **124**, 8626–8643.

- Marsan, D. (2006). Can coseismic stress variability suppress seismicity shadows? Insights from a rate-and-state friction model, *J. Geophys. Res.* **111**, no. B6, doi: [10.1029/2005JB004060](https://doi.org/10.1029/2005JB004060).
- Meade, B. J., P. M. DeVries, J. Faller, F. Viegas, and M. Wattenberg (2017). What is better than Coulomb failure stress? A ranking of scalar static stress triggering mechanisms from 105 mainshock-aftershock pairs, *Geophys. Res. Lett.* **44**, no. 22, 11–409.
- Narteau, C., P. Shebalin, and M. Holschneider (2005). Onset of power law aftershock decay rates in Southern California, *Geophys. Res. Lett.* **32**, L22312, doi: [10.1029/2005GL023951](https://doi.org/10.1029/2005GL023951).
- Narteau, C., P. Shebalin, and M. Holschneider (2008). Loading rates in California inferred from aftershocks, *Nonlinear Processes Geophys.* **15**, 245–263.
- Ogata, Y., and K. Katsura (1993). Analysis of temporal and spatial heterogeneity of magnitude frequency distribution inferred from earthquake catalogs, *Geophys. J. Int.* **113**, 727–738.
- Ohnaka, M. (1983). Acoustic emission during creep of brittle rock, *Int. J. Rock Mech. Min. Sci. Geomech.* **20**, 121–134.
- Omi, T., Y. Ogata, Y. Hirata, and K. Aihara (2013). Forecasting large aftershocks within one day after the main shock, *Sci. Rep.* **3**, 2218.
- Omori, F. (1894). On after-shocks of earthquakes, *J. Coll. Sci. Imp. Univ. Tokyo* **7**, 111–200.
- Page, M. T., N. van der Elst, and S. Hainzl (2024). Testing rate-and-state predictions of aftershock decay with distance, *Seismol. Res. Lett.* doi: [10.1785/0220240179](https://doi.org/10.1785/0220240179).
- Parsons, T. (2006). Tectonic stressing in California modeled from GPS observations, *J. Geophys. Res.* **111**, no. B3, doi: [10.1029/2005JB003946](https://doi.org/10.1029/2005JB003946).
- Peng, Z., J. E. Vidale, and H. Houston (2006). Anomalous early aftershock decay rate of the 2004 Mw6.0 Parkfield, California, earthquake, *Geophys. Res. Lett.* **33**, L17307, doi: [10.1029/2006GL026744](https://doi.org/10.1029/2006GL026744).
- Peng, Z., J. E. Vidale, M. Ishii, and A. Helmstetter (2007). Seismicity rate immediately before and after main shock rupture from high-frequency waveforms in Japan, *J. Geophys. Res.* **112**, no. B3, doi: [10.1029/2006JB004386](https://doi.org/10.1029/2006JB004386).
- Powers, P. M., and T. H. Jordan (2010). Distribution of seismicity across strike-slip faults in California, *J. Geophys. Res.* **115**, no. B5, doi: [10.1029/2008JB006234](https://doi.org/10.1029/2008JB006234).
- Rinaldi, A. P., L. Impropa, S. Hainzl, F. Catalli, L. Urpi, and S. Wiemer (2020). Combined approach of poroelastic and earthquake nucleation applied to the reservoir-induced seismic activity in the Val d'Agri area, Italy, *J. Rock Mech. Geotech. Eng.* **12**, 802–810.
- Scholz, C. H. (1968). Mechanism of creep in brittle rock, *J. Geophys. Res.* **73**, 3295–3302.
- Scholz, C. H. (1998). Earthquakes and friction laws, *Nature* **391**, 37–42.
- Sharma, S., S. Hainzl, G. Zöeller, and M. Holschneider (2020). Is Coulomb stress the best choice for aftershock forecasting? *J. Geophys. Res.* **125**, no. 9, e2020JB019553, doi: [10.1029/2020JB019553](https://doi.org/10.1029/2020JB019553).
- Sharma, S., S. Hainzl, and G. Zöller (2023). Seismicity parameters dependence on main shock-induced co-seismic stress, *Geophys. J. Int.* **235**, no. 1, 509–517.
- Shcherbakov, R., D. L. Turcotte, and J. B. Rundle (2004). A generalized Omori's law for earthquake aftershock decay, *Geophys. Res. Lett.* **31**, L11613, doi: [10.1029/2004GL019808](https://doi.org/10.1029/2004GL019808).
- Sirorattanakul, K., Z. E. Ross, M. Khoshmanesh, E. S. Cochran, M. Acosta, and J.-P. Avouac (2022). The 2020 Westmorland, California earthquake swarm as aftershocks of a slow slip event sustained by fluid flow, *J. Geophys. Res.* **127**, e2022JB024693, doi: [10.1029/2022JB024693](https://doi.org/10.1029/2022JB024693).
- Stein, R. S. (1999). The role of stress transfer in earthquake occurrence, *Nature* **402**, 605–609.
- Toda, S., R. S. Stein, P. A. Reasenberg, J. H. Dieterich, and A. Yoshida (1998). Stress transferred by the 1995, Mw =6.9 Kobe, Japan, shock: Effect on aftershocks and future earthquake probabilities, *J. Geophys. Res.* **103**, 24,543–24,565.
- Toda, S., R. S. Stein, and T. Sagiya (2002). Evidence from the ad 2000 Izu islands earthquake swarm that stressing rate governs seismicity, *Nature* **419**, 58–61.
- Utsu, T., Y. Ogata, and R. Matsu'ura (1995). The centenary of the Omori formula for decay law of aftershock seismicity, *J. Phys. Earth* **43**, 1–33.
- van der Elst, N. J. (2021). *b*-positive: A robust estimator of aftershock magnitude distribution in transiently incomplete catalogs, *J. Geophys. Res.* **126**, e2020JB021027, doi: [10.1029/2020JB021027](https://doi.org/10.1029/2020JB021027).
- van der Elst, N. J., and M. T. Page (2023). *a*-positive: A robust estimator of the earthquake rate in incomplete or saturated catalogs, *J. Geophys. Res.* **128**, e2023JB027089, doi: [10.1029/2023JB027089](https://doi.org/10.1029/2023JB027089).
- Zaliapin, I., and Y. Ben-Zion (2013). Earthquake clusters in southern California I: Identification and stability, *J. Geophys. Res.* **118**, 2847–2864.
- Zaliapin, I., A. Gabrielov, V. Keilis-Borok, and H. Wong (2008). Clustering analysis of seismicity and aftershock identification, *Phys. Rev. Lett.* **101**, 018501.

Manuscript received 6 May 2024

Published online 1 October 2024